Wave-current interaction in nearshore shear instability analyzed with a vortex force formalism

Yusuke Uchiyama,[1] James C. McWilliams,[1] and Juan M. Restrepo[2]

Received 25 September 2008; revised 9 March 2009; accepted 26 March 2009; published 24 June 2009.

[1] We examine wave-current interactions in littoral current shear instabilities above a single-barred beach using a fully coupled wave and barotropic current model based on the multiscale asymptotic theory derived by McWilliams et al. (2004). This Eulerian wave-averaged model captures wave effects on currents (WEC) in a manner that leads to simple interpretations. The dynamically conservative WEC are the vortex force and material transport by Stokes drift and the sea level adjustment by wave set-down and setup. In the setting considered here there are also important current effects on the waves (CEW): induction of a Doppler shift by currents and surface elevation variation in the wave dispersion relation. Nonconservative effects, due to wave breaking and bottom drag, also play a prominent role in generating and equilibrating the mean alongshore current, consistent with prior studies. High bottom drag stabilizes the currents, while a drag reduction below a critical threshold value leads to shear instability with nearly periodic, alongshore-fluctuating eddies. An even smaller bottom drag yields irregular eddy motions with intermittent offshore eruption of vortex pairs from the meandering alongshore current. Several alternative parameterizations of the bottom drag are contrasted here. Including CEW in the model leads to a delay in the onset of the instability, a suppression of fluctuations in cross-shore velocity and lateral Reynolds stress, and an enhancement of the mean alongshore velocity. The WEC increase the Reynolds stress in the offshore region, and the conservative vortex force and mean advection are comparable in magnitude to the breaking acceleration and bottom drag. Conversely, the CEW reduce the Reynolds stress and attenuate the breaking acceleration through refractive focusing by current shear. Overall, the WEC enhance the instantaneous cross-shore momentum flux to induce more energetic eddy motions and retard the mean alongshore current, while the CEW stabilize the fluctuations and help maintain a strong mean current.

Citation: Uchiyama, Y., J. C. McWilliams, and J. M. Restrepo (2009), Wave-current interaction in nearshore shear instability analyzed with a vortex force formalism, *J. Geophys. Res.*, *114*, C06021, doi:10.1029/2008JC005135.

1. Introduction

[2] We investigate littoral currents induced by wave breaking using a barotropic model with a barred beach topography. Our focus is the horizontal shear instability of the alongshore current, often called a "shear wave" for its propagating behavior. Shear waves were first observed by *Oltman-Shay et al.* [1989] during the SUPERDUCK field experiment, and they have been modeled as an inflection point, normal mode instability of a specified alongshore current profile $V(x)$ [cf. *Bowen and Holman*, 1989; *Dodd et al.*, 1992, 1994, 2000; *Reniers et al.*, 1997]. Here, x is a beach-normal coordinate. The instability is observed to be stronger on barred beaches than on planar beaches. A numerical study with time-dependent, rigid lid, nonlinear shallow water equations and an initial $V(x)$ shows that fully developed shear waves alter the mean alongshore current profile significantly and eventually limit the growth of the instabilities [*Allen et al.*, 1996; *Slinn et al.*, 1998]. *Özkan-Haller and Kirby* [1999] and *Noyes et al.* [2005] obtain better agreement with measurements of the growth rate and the propagation speed of the resulting shear instability waves with a breaking-generated current over a barred topography and a refracting wave field. They employ nonlinear shallow water equations with phase-averaged surface gravity wave effects on currents (WEC), using forcing terms represented by the divergence of the radiation stress tensor [*Longuet-Higgins and Stewart*, 1962; *Longuet-Higgins*, 1970a, 1970b]. *Özkan-Haller and Li* [2003] (hereinafter referred to as OL03) couple a similar current model to a WKB wave number refraction, action conservation wave model with parameterized wave breaking [*Thornton and Guza*, 1983]. Effects of the currents on the waves (CEW) by Doppler shifting in the dispersion relation are

[1] Institute of Geophysics and Planetary Physics, University of California, Los Angeles, California, USA.
[2] Departments of Mathematics and Physics, University of Arizona, Tucson, Arizona, USA.

0148-0227/09/2008JC005135$09.00

included. *Kennedy and Zhang* [2008] perform a linear stability analysis including both radiation stress and Doppler shifting. Phase-resolving models have also been utilized in solving the flow, without any distinction between waves and currents, to investigate vorticity transport in nearshore circulations [e.g., *Bühler and Jacobson*, 2001; *Chen et al.*, 2003; *Terrile et al.*, 2008].

[3] OL03 show that when the bottom drag has intermediate strength, leading to a marginally unstable shear flow, the interaction of waves and currents results in a reduction in the offshore extent of the currents; a delay in the onset of the instability; and an increase of the alongshore shear wave propagation speed. Most of these effects are minimal in a more turbulent regime with weaker bottom drag, but the offshore extent of the eddy mixing remains suppressed to some degree. OL03 attribute these effects to refraction and energy gain from the incident waves around offshore-directed flows associated with the shear instabilities. *Newberger and Allen* [2007] extend OL03 using the same refraction wave model and the three-dimensional, primitive equation current model with depth-averaged WEC terms. They qualitatively demonstrate that CEW tends to suppress shear instability in a relatively high bottom friction regime.

[4] The primary purpose of this paper is to analyze how the littoral current and its shear instability are determined by the various WEC and CEW mechanisms. We will employ an Eulerian, multiscale wave-current framework, based on the asymptotic equations derived by *McWilliams et al.* [2004] (hereinafter referred to as MRL04). This has a vortex force formalism that cleanly separates conservative and nonconservative WEC mechanisms (unlike the radiation stress formalism). *Lane et al.* [2007] analyze how the radiation stress formalism [*Longuet-Higgins and Stewart*, 1964; *Longuet-Higgins*, 1970a, 1970b; *Hasselmann*, 1971] relates to the vortex force formalism; also see *Smith* [2006]. Section 2 describes the wave-current interaction model that includes nonconservative effects of wave breaking and bottom drag; section 3 presents the essential mean wave and current structures. Since previous studies have shown that bottom drag plays a critical role in nearshore shear instability, a secondary purpose of this paper is to determine how the shear wave evolution and pattern differ with different parameterization formulas for the bottom drag (section 4). Section 5 analyzes the various wave-current interactions in the nonlinear regime.

2. Wave-Current Interaction Model

[5] We choose a west coast configuration with (x, y) positive to the (east, north), and $x = 0$ as the shoreline; $\xi = -x > 0$ is the offshore distance. To facilitate comparisons with previous studies, we consider a simple, alongshore uniform topography, inspired by the field campaigns at Duck, NC. The offshore resting ocean depth profile is

$$h(\xi) = 0.015\xi + 2.08\tanh[0.017\xi] - 2.5\exp\left[-0.001(\xi - 100)^2\right] \tag{1}$$

(Figure 1a), with an added constraint of $h \geq 0.1$ m. The swash zone is excluded since runup is reported to have a negligible effect on shear instabilities [*Özkan-Haller and Kirby*, 1999]. The cross-shore and alongshore lengths of the domain are set to 512 m (about four times the width of the surf zone) and 768 m (about six to eight wavelengths of shear waves in the marginally unstable regime). The computational grid is uniform with a spacing of 2 m.

[6] In this region the waves have a typical period of tens of seconds. The spectra are somewhat narrow-banded, and their dynamics is weakly nonlinear outside the breaking zone. The temporal scales of interest for the alongshore currents and shear waves are hundreds of seconds or more, longer than that of the primary wave oscillations. This motivates a wave-averaged theoretical framework. We neglect the Coriolis force as dynamically relevant only on longer time scales.

[7] The currents are assumed to be barotropic, and they impart a Doppler shift to the wave frequency. The wave-averaged water column depth is time-varying because of sea level changes from the dynamic pressure of the currents (including the so-called "wave setup" caused by nonconservative wave effect through wave breaking) as well as the quasi-static response (see MRL04) that we may alternatively call "wave set-down" where waves are weaker. The Doppler shift and depth variation are the CEW elements. The dynamically conservative elements in the WEC are this quasi-static response; the vortex force that combines the total flow vorticity and the Stokes drift velocity; and the material advection by the Stokes drift. The nonconservative element in the WEC is parameterized wave breaking. The computational time step size is around $\Delta t = 0.1$ s, consistent with the CFL criterion for the current and barotropic gravity wave speeds with our fine grid spacing.

2.1. Currents

[8] MRL04 derive a multiscale asymptotic model for the phase-averaged, conservative dynamical effects of surface gravity waves on currents and infragravity waves with slowly varying space and time scales using a "vortex force" formalism [e.g., *Craik and Leibovich*, 1976; *McWilliams et al.*, 1997; *McWilliams and Restrepo*, 1999]. The dynamical equation for infragravity waves driven by primary short waves derived in MRL04 is implemented in a numerical coastal ocean model to investigate generation and propagation of infragravity wave in the deep ocean in the context of seismic hum excitation [*Uchiyama and McWilliams*, 2008]. To extend this, assuming barotropic currents, the equations for the horizontal current and dynamic sea level height ζ are

$$\frac{\partial \zeta}{\partial t} + \nabla \cdot H\mathbf{u} = -\frac{\partial \hat{\zeta}}{\partial t} - \nabla \cdot \mathbf{U}^{St}, \tag{2}$$

$$\frac{\partial \mathbf{u}}{\partial t} + \mathbf{u} \cdot \nabla \mathbf{u} + g\nabla\zeta - \mathbf{J} = \mathbf{B} - \mathbf{D} + R\nabla^2\mathbf{u}, \tag{3}$$

where g is gravitational acceleration; $\mathbf{u} = (u, v)$ is the depth-averaged Eulerian current velocity; $\chi = \partial v/\partial x - \partial u/\partial y$ is its vorticity; $H = h + \zeta^c$ is the local water column depth; $\zeta^c = \zeta + \hat{\zeta}$ is the composite sea level elevation; $\hat{\zeta}$ is the quasi-static response due to the conservative WEC specified

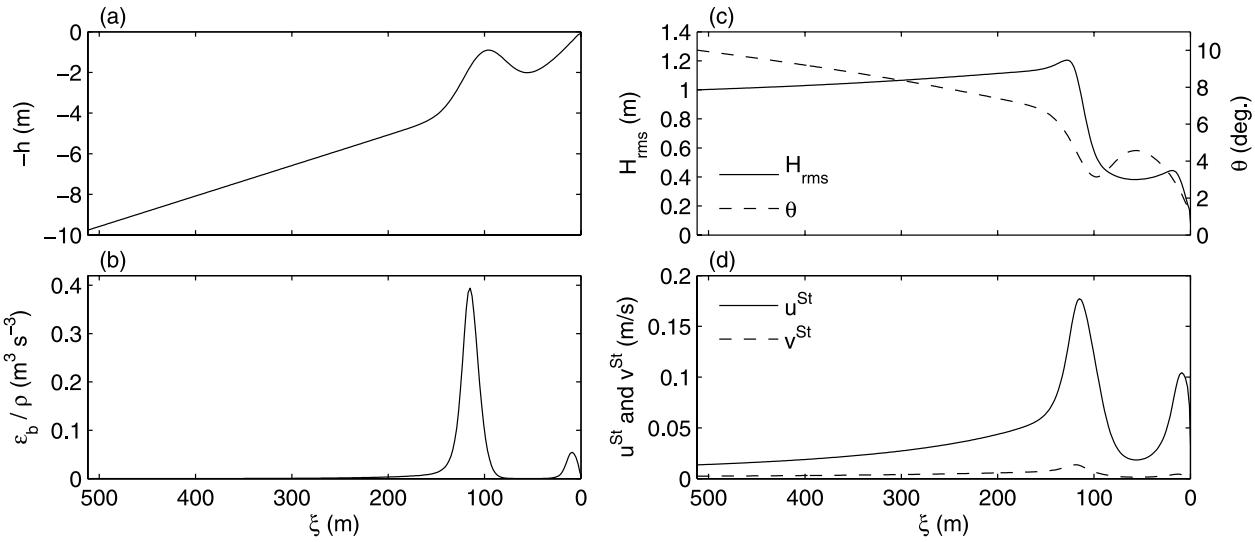

Figure 1. (a) The single-barred bottom topography $h(\xi)$ from (1) with an offshore bar crest at $\xi = 100$ m. (b) Breaking wave dissipation function $\epsilon_b(\xi)$ from (16). (c) RMS wave height $H_{rms}(\xi)$ and wave angle $\theta(\xi)$ and (d) Stokes velocity $\mathbf{U}^{St}/H$ from (11). The offshore wave parameters are $H_{rms} = 1.0$ m, peak period $T_p = 10$ s, and peak direction $\theta_m = 10°$.

in the subsequent subsection; $\mathbf{U}^{St}$ is Stokes transport (i.e., vertically integrated Stokes drift velocity $\mathbf{u}^{St}$); and

$$\mathbf{J} = \left(J_x, J_y\right) - \hat{\mathbf{z}} \times \frac{1}{H}\mathbf{U}^{St}\chi \tag{4}$$

is the vortex force. t is time; $\mathbf{x} = (x, y)$ are horizontal coordinates; and the vertical coordinate z is aligned with gravity. Note that the relation of the present formalism to the conventionally used radiation stress formalism is given by *Smith* [2006]. The right side of the momentum equation contains the parameterized nonconservative processes. Acceleration due to wave breaking is

$$\mathbf{B} = \left(B_x, B_y\right) = \frac{\epsilon_b \mathbf{k}}{\rho H \sigma}. \tag{5}$$

where ϵ_b: wave energy dissipation rate due to depth-induced breaking, $\mathbf{k}$: wave number vector, and σ: the intrinsic wave frequency. Lateral diffusion with eddy viscosity $R = 0.1$ m^2 s^{-1} is used throughout the present study to stabilize the numerical solutions in the eddying regime. The bottom drag force is

$$\mathbf{D} = \left(D_x, D_y\right) = \frac{\boldsymbol{\tau}_b}{\rho H}, \tag{6}$$

with ρ the fluid density and $\boldsymbol{\tau}_b$ the bottom stress (chosen as one of several alternatives; section 4).

[9] The bottom drag $\mathbf{D}$ plays a crucial role in the appearance and maintenance of alongshore currents. We consider three different parameterization models for the bottom stress $\boldsymbol{\tau}_b$. The first model is a linear drag law:

$$\boldsymbol{\tau}_b = \rho\mu\mathbf{u}, \tag{7}$$

with a constant linear drag coefficient μ [m s^{-1}]. The second model is a combined wave and current drag proposed by *Soulsby* [1995]:

$$\boldsymbol{\tau}_b = \boldsymbol{\tau}_c\left[1.0 + 1.2\left(\frac{|\tau_w|}{|\tau_w| + |\boldsymbol{\tau}_c|}\right)^{3.2}\right], \tag{8}$$

$$\boldsymbol{\tau}_c = \rho\left[\frac{\kappa}{\ln(z_m/z_o)}\right]^2 |\mathbf{u}|\mathbf{u};\ \ |\tau_w| = \frac{1}{2}\rho f_w |\mathbf{u}_b^w|^2, \tag{9}$$

where $\boldsymbol{\tau}_c$ and τ_w are bottom stresses due to current and waves [Pa]; κ is the von Kármán constant; z_m is a reference depth above the bed (in the barotropic model we simply define $z_m = H/2$) and z_o is bed roughness length [m]; f_w is the wave friction factor given by $f_w = 1.39(\sigma z_o/|\mathbf{u}_b^w|)^{0.52}$ [*Soulsby*, 1997]; and $|\mathbf{u}_b^w| = \sigma A/\sinh kH$ is the wave orbital velocity at the bottom. The third alternative is another combined wave-current, bottom drag model originally proposed by *Feddersen et al.* [2000] based on data obtained at Duck, NC:

$$\boldsymbol{\tau}_b = 0.015\boldsymbol{\rho}\left(\frac{k_a}{H}\right)^{1/3}\left[(1.16)^2 + \left(\frac{|\mathbf{u}|}{|\mathbf{u}_{rms}^w|}\right)^2\right]^{1/2} |\mathbf{u}_{rms}^w|\mathbf{u}, \tag{10}$$

where $\mathbf{u}_{rms}^w = \mathbf{u}_b^w / \sqrt{2}$ is the RMS wave orbital velocity and $k_a = 0.0125$ is the apparent roughness (m) [*Ruessink et al.*, 2001]. Notice that *Feddersen et al.* [2000] only parameterized the quadratic velocity moment for the alongshore momentum balance, while we crudely presume here that the model is expandable to the two-dimensional fields.

[10] All the governing equations are transformed to curvilinear horizontal coordinates and implemented into a

barotropic version of Regional Ocean Modeling System (ROMS [e.g., *Shchepetkin and McWilliams*, 2005]) so that we can make use of its features including capability of parallel computing and the reflection-free open-boundary schemes. All fields are y periodic. At the offshore edge, radiation conditions [*Flather*, 1976] are applied with a nudging toward $\zeta = 0$, $v = 0$, and $u = -U^{St}/H$. At the nearshore boundary, there is a zero normal mass flux, $u + u^{St} = 0$; no tangential flow, $v = 0$; and the Neumann condition, $d\zeta/dx = 0$. $\mathbf{u}^{St} \approx 0$ near the shoreline because of wave dissipation by breaking.

2.2. Waves

[11] In accordance with MRL04 for a monochromatic surface wave field, the Stokes transport $\mathbf{U}^{St}$ and quasi-static response $\hat{\zeta}$ are

$$\mathbf{U}^{St} = \frac{A^2\sigma\mathbf{k}}{2k\tanh kH} = \mathcal{A}\mathbf{k};\ \hat{\zeta} = -\frac{A^2k}{2\sinh 2kH}. \tag{11}$$

k is the magnitude of $\mathbf{k}(\mathbf{x}, t)$; $A(\mathbf{x}, t)$ is the wave amplitude; and $\mathcal{A}$ is the wave action. This expression is for nonbreaking, small wave slope waves that may not be true in the surf zone; however, we simply assume that (11) is approximately applicable to the problem considered here. Note that the same assumption is also implied for other WEC models such as the radiation stress model. In the nearshore setting under consideration, the wave field is well captured by this slowly varying envelope representation and exhibits very weak nonlinearity (OL03 and references therein). So, A can be related to a field observable RMS wave height H_{rms} and $\mathbf{k}$ to the spectrum peak wave number. Notice that $\hat{\zeta}$ is a quasi-static quantity, unrelated to any currents. In terms of the wave action $\mathcal{A} = E/\sigma$, where $E = \frac{1}{2}\rho g A^2 = \frac{1}{8}\rho g H_{rms}^2$, the "ray theory" evolution equations for the wave field are

$$\frac{\partial\mathcal{A}}{\partial t} + \nabla\cdot\left(\mathcal{A}\mathbf{c}_g\right) = -\frac{\epsilon_b}{\sigma}, \tag{12}$$

$$\frac{\partial\mathbf{k}}{\partial t} + \mathbf{c}_g\cdot\nabla\mathbf{k} = -(\mathbf{k}\cdot\nabla)\mathbf{u} - \frac{k\sigma}{\sinh 2kH}\nabla h, \tag{13}$$

$$\sigma^2 = gk\tanh kH; \quad \omega = \mathbf{u}\cdot\mathbf{k} + \sigma, \tag{14}$$

where ω is the wave frequency. The wave group velocity is

$$\mathbf{c}_g = \mathbf{u} + \frac{\sigma}{2k^2}\left(1 + \frac{2kH}{\sinh 2kH}\right)\mathbf{k}. \tag{15}$$

The parameterized, depth-integrated rate of wave energy loss due to breaking ϵ_b [*Thornton and Guza*, 1983] is

$$\epsilon_b = \frac{3}{16}\sqrt{\pi}\rho g\frac{B_r^3}{\gamma^4 H^5}\frac{\sigma}{2\pi}H_{rms}^7 \geq 0, \tag{16}$$

$B_r = 0.8$, and $\gamma = 0.4$. Thus, the CEW occurs in (12)–(16) when $\mathbf{u} \neq 0$ and $H \neq h$. At the offshore boundary, incident $\mathcal{A}$ and $\mathbf{k}$ are specified, while at the nearshore boundary zero-gradient, Neumann conditions are used.

2.3. Three Types of WEC/CEW Model Setup

[12] To better characterize the dynamical roles played by waves and currents in the alongshore current shear instability, we exploit the relatively clean separation of wave and current effects in our formulation by defining three types of model calculations:

[13] 1. The WEC+CEW model uses full model computations (as in the preceding two subsections).

[14] 2. The WEC-only model uses full current model computations but with no Doppler shift, i.e., $\mathbf{u} = 0$ and $H = h$ in the wave model (while $H = h + \zeta^c$ in the current model).

[15] 3. The NW model excludes the conservative WEC and CEW terms while retaining the background wave-breaking effects, namely,

$$\frac{\partial\zeta}{\partial t} + \nabla\cdot H\mathbf{u} = 0, \tag{17}$$

$$\frac{\partial\mathbf{u}}{\partial t} + \mathbf{u}\cdot\nabla\mathbf{u} + g\nabla\zeta = \mathbf{B}^{NW} - \mathbf{D} + R\nabla^2\mathbf{u}, \tag{18}$$

with $\mathbf{B}^{NW} = (0, B_y^{NW})$, $B_y^{NW} = \epsilon_b k_y/\rho H\sigma$, where ϵ_b, $\mathbf{k}$, and σ are determined from steady state wave solutions without the CEW. This NW model lacks Stokes drift and wave setup/set-down, and it does not develop a cross-shore anti-Stokes flow (see section 2.4). Notice that we neglect the cross-shore forcing B_x^{NW} in the NW model as *Allen et al.* [1996] did, whereas it could be easily incorporated giving a wave setup that might make results slightly different.

[16] For large τ_b all three models yield steady, stable, alongshore-uniform (i.e., one-dimensional (1-D)) solutions. One-dimensional solutions also exist for any τ_b, and they can be calculated by integrating the models without alongshore variation to steady state. In practice, this is achieved by restricting the number of the alongshore grid points to two, instead of 384 points for the two-dimensional (2-D) runs. To initialize the 2-D integrations, the 1-D steady solutions are utilized for 2-D WEC+CEW and WEC-only runs. For 2-D NW runs, we calculate $B_y^{NW}(x)$ and $v(x)$ from the 1-D steady WEC-only model. Then small perturbations are imposed in the u and v fields.

2.4. Mean Continuity and Momentum Balances

[17] We now derive mean balance equations for the currents, averaging in time and alongshore coordinate (assuming y periodicity). We use a Reynolds decomposition; that is, for any $f(x, y, t)$, $f(x, y, t) = \langle f\rangle + f'$, with $\langle f'\rangle = 0$, and the averaging period is typically greater than an hour.

[18] In the presence of wave and current fluctuations, the mean continuity balance can be integrated (2) in x from the shoreline to yield

$$\langle H\rangle\langle u\rangle + \langle H'u'\rangle + \left\langle U^{St}\right\rangle = 0. \tag{19}$$

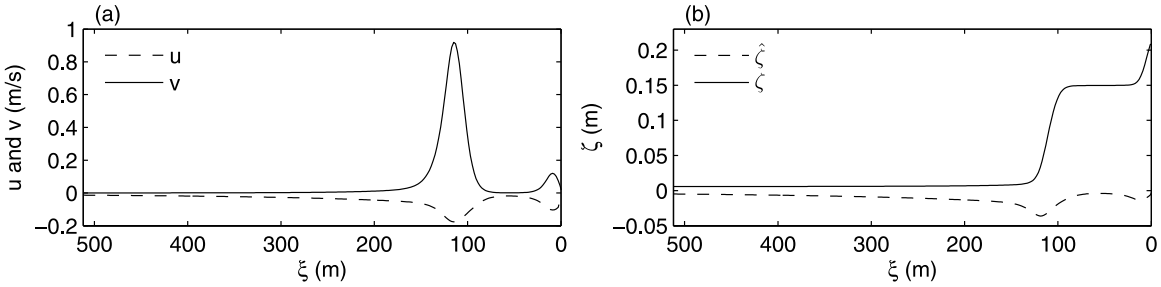

Figure 2. Nearshore steady 1-D (a) currents and (b) sea level with WEC (but not CEW) for the topography and wave profiles in Figure 1. Also shown in Figure 2b is the quasi-static response $\hat{\zeta}(\xi)$.

For steady waves and currents, this implies anti-Stokes flow, $\langle u \rangle = -\langle u^{St} \rangle$. The mean momentum balance in the alongshore direction is

$$\langle u \rangle \frac{\partial \langle v \rangle}{\partial x} + \left\langle u' \frac{\partial v'}{\partial x} \right\rangle + \langle u^{St} \rangle \langle \chi \rangle + \langle u^{St\prime} \chi' \rangle + \mu \left\langle \frac{v}{H} \right\rangle - \langle B_y \rangle = 0. \tag{20}$$

Here for didactic purposes we have used the linear bottom drag model and ignored small lateral diffusion. In (20) $\langle u \rangle$ is zero if the Stokes drift is zero. If the flow is steady, the breaking and bottom drag terms balance:

$$\mu \left\langle \frac{v}{H} \right\rangle = \langle B_y \rangle. \tag{21}$$

This force balance is the classical dynamical conception of a littoral current [*Longuet-Higgins*, 1970a, 1970b]. Instead, if the Stokes drift is nonzero and we still assume there are no current fluctuations, the mean advection cancels the mean vortex force because of the anti-Stokes flow; that is,

$$\langle u \rangle \partial_x \langle v \rangle = -\langle u^{St} \rangle \langle \chi \rangle, \tag{22}$$

where ∂_x denotes $\partial/\partial x$. So (21) applies in general for steady alongshore currents, even though (22) was not originally envisioned as part of the classical conception. An example for the steady state alongshore momentum balance diagnosed with a 1-D littoral current solution is illustrated later in Figure 3. For unsteady (unstable) currents and waves, both the fluctuation advection (i.e., eddy Reynolds stress divergence) and the fluctuation vortex force may contribute as shown later. Similarly, the mean y momentum balance for the NW model (18) is

$$\left\langle u' \frac{\partial v'}{\partial x} \right\rangle - \left\langle B_y^{NW} \right\rangle + \mu \frac{\langle v \rangle}{H} = 0. \tag{23}$$

[19] Provided that there is no mean surface elevation (e.g., tide), wave setup ζ can be obtained from the mean cross-shore momentum balance dominated by its pressure gradient force and the breaking acceleration,

$$g \partial_x \langle \zeta \rangle \approx \langle B_x \rangle. \tag{24}$$

By integrating (24) and including the conservative quasi-static response $\langle \hat{\zeta} \rangle$, the composite actual sea level $\langle \zeta^c \rangle$ is approximately retrieved [e.g., *Longuet-Higgins and Stewart*, 1962; *Bowen et al.*, 1968].

3. Steady Wave-Driven Current

3.1. Cross-Shore Profiles

[20] To obtain a specific solution, we specify the incident wave conditions typical of those measured at Duck, NC [*Church and Thornton*, 1993]; RMS wave height H_{rms} = 1.0 m, peak period T_p = 10 s, and peak direction $\theta_m = 10°$ away from the shore-normal direction. This generates alongshore currents in the positive y direction for all cases. We assume the waves are steady, ignore CEW for now (i.e., WEC-only model), and show cross-shore one-dimensional steady state solutions.

[21] With shoaling barred topography (Figure 1a), wave steepening and refraction occur (Figure 1c) as expected. The RMS wave height H_{rms} gently amplify and steepen until around ξ = 120 m where breaking begins slightly offshore from the bar crest in accordance with breaking dissipation ϵ_b (Figure 1b). The secondary breaking is also depicted near the shoreline. The Stokes drift is strongly shoreward and more weakly in the alongshore direction (Figure 1d) because of the small wave angle θ (Figure 1c).

[22] The steady 1-D currents and sea level with the linear bottom drag coefficient (μ = 0.006 m s^{-1}) are shown in Figure 2. The alongshore current $v(\xi)$ has approximately the shape of the breaking acceleration **B** multiplied by H, as required by the balance (21). The cross-shore current $u(\xi)$ is an anti-Stokes flow, $-u^{St}(\xi)$ (section 2.4). $\hat{\zeta}(\xi)$ manifests a weak wave set-down around the breaking region and a much stronger onshore wave setup in ζ as H_{rms} drops toward zero (Figure 2) [e.g., *Bowen et al.*, 1968] as approximated by (24). The result shown here is qualitatively consistent with the previous works [e.g., *Longuet-Higgins*, 1970a, 1970b; *Thornton and Guza*, 1986; *Raubenheimer et al.*, 2001]

3.2. Alongshore Momentum Balance and Roles of WEC and CEW

[23] In the 1-D steady solution with the WEC+CEW model with μ = 0.006 m s^{-1}, the mean alongshore momentum balance for the same incident wave condition as in section 3.1 (Figure 3) shows that the forces are concentrated in the two breaking zones, near the bar and near the

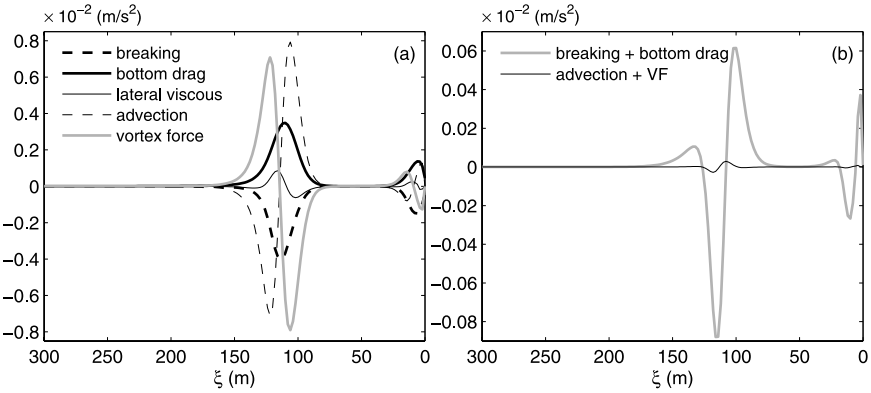

Figure 3. Steady 1-D solutions for the WEC+CEW model with linear bottom drag near the critical value for instability (μ = 0.006 m s^{-1}): (a) terms in the y momentum balance (20) (excluding contributions from fluctuations) and (b) differences between the advection and vortex force and between the breaking acceleration and bottom drag terms. Notice the change of scale between the plots.

shoreline. In each zone the principal contributions are from breaking acceleration, mean advection, mean vortex force, and bottom drag, and they are all comparable in magnitude. Since this is a steady case, the two subbalance relations (21) and (22) hold separately, except for relatively small corrections due to lateral momentum diffusion. Breaking accelerates the mean alongshore current and bottom drag quenches it (note that the plotted terms are negative forces). The vortex force acts to move the current toward the shoreline, and mean momentum advection by the anti-Stokes flow acts to push it further offshore.

[24] The 1-D solutions are further illustrated for models with the WEC and either with or without the CEW (Figure 4). The wave height is rather similar to each other; however, we see an enhanced wave height and stronger anti-Stokes offshore flow, $u < 0$ inshore of the bar, because of the wave-steepening Doppler shift from the latter with the CEW. OL03 did not show a similar comparison and merely denoted that the CEW has little effect on these result. They assumed that the Doppler shift takes place on Lagrangian current that implies zero cross-shore flow, whereas it occurs on Eulerian current (i.e., $u \neq 0$) in the present study. Hence, the alteration in H_{rms}, u^{St} and u in OL03 is considered to be much less than the present result. The wave setup effect in sea level ζ^c further adds to the CEW differences in H_{rms} and u; ζ^c in the WEC-only solution is very similar to the WEC+CEW solution (not shown), except for an increase of about 1 cm in the runnel (i.e., the trough behind the bar). This contrast between WEC+CEW and WEC-only cases is essentially the same as that will be found in the 2-D unstable solution shown later in section 5. In the 1-D NW model $u = 0$, of course, and H_{rms} is the same as in the WEC-only model but is only relevant as a basis for calculating B_y^{NW}. The alongshore current v is quite similar in 1-D solutions for the different models (also not shown).

4. Alternative Bottom Drag Formulations

[25] Several parameterizations for the bottom drag have been proposed. Here we show how the alongshore shear instability outcome qualitatively changes depending on the magnitude of the drag coefficient, but it has less dependence on the particular parameterization form used. We use the full wave-current model specified in section 2.

[26] We consider a total of eight cases. In all cases the incident wave conditions are the same as those in section 3. The first six cases illustrate the dependence on the coefficient in the linear drag model (7), with values that range between μ = 0.002–0.007 m s^{-1}. The two other cases are the wave-enhanced drag models in (8) and (10). All the 2-D simulations are initiated with the corresponding 1-D, alongshore uniform, steady wave and current fields with small perturbations imposed in u and v. Notice that the results shown below are essentially equivalent to those drawn by *Allen et al.* [1996], *Özkan-Haller and Kirby* [1999], and

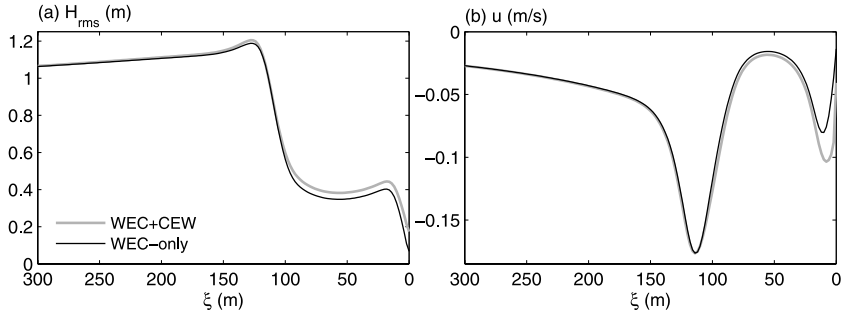

Figure 4. Steady profiles in WEC+CEW (light line) and WEC-only (heavy line) 1-D solutions: (a) wave height H_{rms} and (b) u. These cases have a linear drag with μ = 0.006 m s^{-1}.

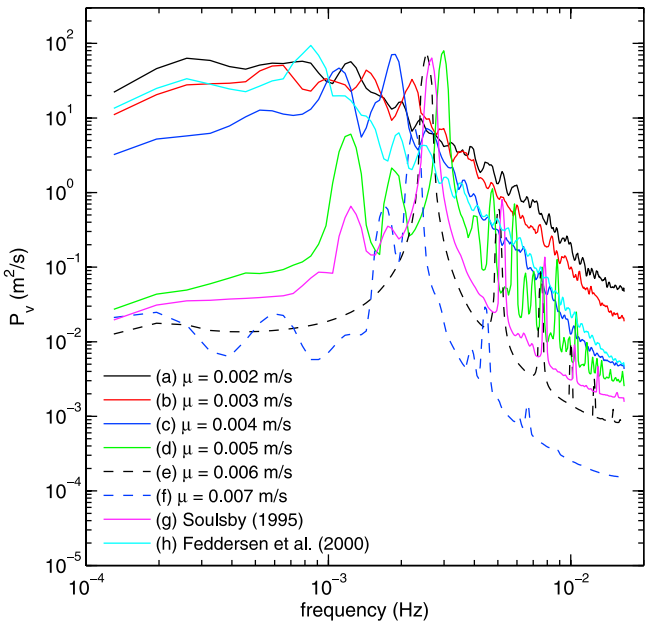

Figure 5. Alongshore-averaged frequency spectra for the fluctuating component of alongshore velocity v' at the bar crest for eight different bottom drags in the WEC+CEW model. Spectra are calculated from the last 4.2 h of the integration.

OL03, while we use the different formalism and two wave-enhanced bottom drag models (section 2) additionally.

4.1. Unstable Fluctuations

[27] Figure 5 shows the frequency spectra of the fluctuating component of alongshore velocity $v' = v - \langle v \rangle$ at the bar crest (ξ = 100 m) for the eight cases, a–h. The linear drag model makes it apparent that a smaller drag leads to a much broader range of unstable modes, particularly in the high-frequency band, as shown by *Allen et al.* [1996] and *Özkan-Haller and Kirby* [1999]. We denote flows such as those in cases a–c as "turbulent" and cases d–f as "marginally unstable" ("weakly nonlinear" regime in the work by *Feddersen* [1998] with harmonics at multiples of the peak frequency), distinguishing between them by the breadth of the frequency spectrum. The marginal regime corresponding to higher drag is typified by the cases with μ = 0.005 to 0.007 m s^{-1} and with Soulsby model (8). These have narrow-banded spectra with distinct peaks at around $2–3 \times 10^3$ Hz (periods of 330–500 s). The turbulent regime occurs with low drag (i.e., μ = 0.002 to 0.004 m s^{-1}) and with the Feddersen model (10). These cases have more energetic, broad-banded spectra. The behavior of v' with combined wave and current drag in cases g and h is qualitatively similar to those with the linear drag. The Soulsby model has a behavior closest to that of the linear drag case with μ = 0.006 m s^{-1}, and the Feddersen model is closest to the cases with μ = 0.003 or 0.004 m s^{-1}.

4.2. Mean Fields

[28] Now consider the time- and alongshore-averaged fields in the presence of the unstable fluctuations (Figure 6). The averaged wave properties, $\langle u \rangle$ and $\langle \zeta \rangle$ are about the same for all the cases (e.g., Figures 1 and 2) and thus not shown here. The alongshore flow $\langle v \rangle(\xi)$ has its primarily maximum near the bar and a secondary maximum in the nearshore breaking zone. It shows significant changes with μ, broadening as the bottom drag weakens. The vorticity $\langle \chi \rangle$ has a strongly decreasing magnitude with decreasing drag since the alongshore current broadens. These two profile changes are a consequence of increasing lateral eddy momentum flux due to the shear instabilities, consistent with the increasing TKE and Reynolds stress amplitudes as drag decreases. The Soulsby and Feddersen drag cases are less productive in TKE and $-\langle u'v' \rangle$ than the linear drag cases because their bottom drag locally intensifies where $\langle v \rangle$ and $\langle H_{rms} \rangle$ are both large near the breaking point, suppressing fluctuation amplitude and momentum flux.

5. Roles of Waves and Currents in Shear Instability

5.1. Mean Fields

[29] To second order in fluctuation amplitude, the 2-D mean momentum balance is the same as for the 1-D model (Figure 3), but in cases even only somewhat past the marginally critical value of bottom drag the fluctuation contributions become significant and are reflected in the alongshore current $\langle v \rangle$ and its differences due to the WEC and CEW (Figure 7a). The peak $\langle v \rangle$ (and thus $\langle \chi \rangle$) values are largest for the WEC+CEW model, intermediate in the NW model, and least in the WEC-only model. The decrease of the peak in $\langle v \rangle$ due to exclusion of the CEW is by about 10% and that due to exclusion of the WEC is by about 4%. The intensity and effects of the unstable fluctuations, measured in terms of u'_{rms} and Reynold stresses, are greatest for WEC-only, then NW, then WEC+CEW solutions in the offshore region near the bar. Thus, there is an inverse correlation between eddy activity and mean flow there. In particular, the CEW act to weaken the eddies, especially in the cross-shore direction. Near the shoreline strong fluctuations arise only in the WEC+CEW model, although they have almost no effect there on $\langle v \rangle$ since the Reynolds stress is small. Thus, the shoreline fluctuations are not generated by a local shear instability, but rather arise from the CEW modulation of the breaking acceleration (section 5.5).

[30] In the turbulent regime differences among the three types of models are less pronounced than in the marginal regime, although most of them are still evident (Figures 7d–7f). The WEC-only model has the least intense peaks in $\langle v \rangle$ and the strongest Reynolds stress in the offshore breaking region. The role of the CEW is still evident in weakening the offshore eddy Reynolds stress, limiting the offshore extent of the fluctuations in u'_{rms}, and supporting strong fluctuations near the shoreline.

[31] In summary for both regimes, the WEC-only model has the most intense eddy Reynolds stress in the breaking region among the three cases. Incorporation of the CEW causes the attenuation of Reynolds stress and the eddy fluctuations, particularly for u except in the shoreline region where it has the opposite effect. Thus, the peak $\langle v \rangle$ is weakest and the alongshore current width greatest in the

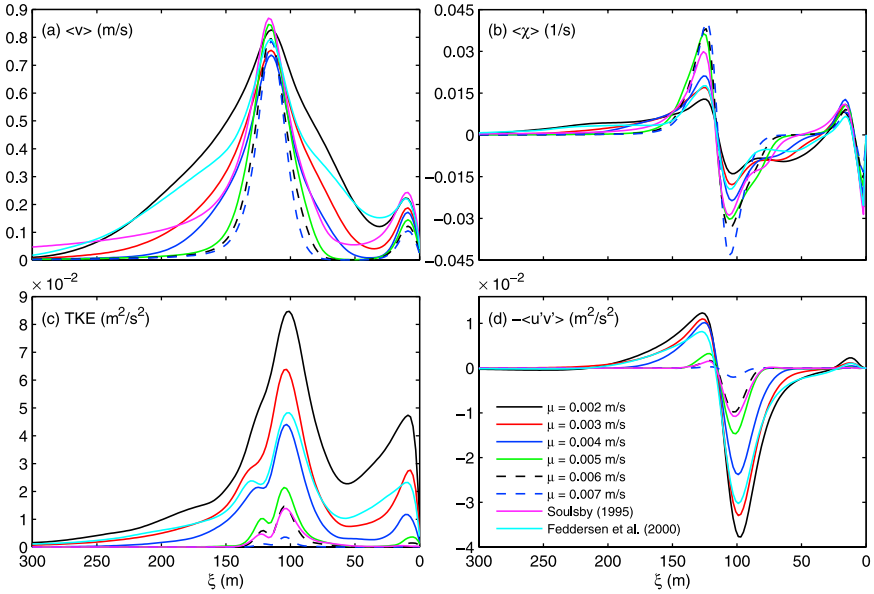

Figure 6. Time- and alongshore-averaged quantities in the WEC+CEW model with different drag parameterizations: (a) alongshore velocity $\langle v \rangle$, (b) vorticity $\langle \chi \rangle$, (c) turbulent kinetic energy (TKE), and (d) off-diagonal component of Reynolds stress $-\langle u'v' \rangle$ for eight different bottom drags (see legend in Figure 6d). The time average is for the last hour in a 6-h integration.

WEC-only model because it has the most energetic eddy momentum fluxes.

5.2. Alongshore Momentum Balance

[32] Cross-shore profiles of the terms in the mean alongshore momentum balances (20) and (23) for the three model formulations are shown in Figures 8 and 9 for 2-D unstable solutions. As in the 1-D steady WEC+CEW solution (Figure 3), the primary balance occurs among the breaking acceleration, bottom drag, mean advection, and mean vortex force. The fluctuation advection (Reynolds stress divergence) has a moderate contribution to the momentum budget in the marginal regime, and it even becomes comparable to the bottom drag as a retardant of breaking acceleration in the turbulent regime. The lateral viscosity and fluctuating vortex force play minor roles in the mean momentum budget, the former by design.

[33] The WEC+CEW model has the smallest breaking momentum production within the bar region while the NW model has the largest near the shoreline. The $\langle B_y \rangle$ terms for the WEC-only and NW models are nearly identical, as expected. Inclusion of CEW leads to a reduction in $\langle B_y \rangle$ around the breaking point by 6% (marginal) or 15% (turbulent) and an enhancement near the shoreline by 10% (marginal) or 4% (turbulent) compared to the WEC-only model. This is caused by changes in the local depth ($H = h + \zeta^c$ for the WEC+CEW model, but $H = h$ for WEC-only) in the wave field (H_{rms}, $\mathbf{k}$ and ϵ_b) since $\mathbf{B}$ is proportional to H^{-5} and H_{rms}^7 according to (16). Mean bottom drag is less in the WEC-only model since $\langle v \rangle$ is less (Figure 7), but it is greater in the NW model because of the lack of reduction of H without wave setup/set-down, especially inshore of the bar (Figure 6). Relative to the NW model, inclusion of the WEC diminishes the y component of the drag by 7.6% in the marginal regime and 16.5% in the turbulent regime in the vicinity of the breaking point.

[34] The mean advection and mean vortex force in the WEC+CEW model are larger than those in the WEC-only model in the marginal regimes, while essentially the same in the turbulent regime. In the NW model $\langle u \rangle$ remains small in the unstable regime, even though it does not need to vanish if the cross-shore eddy mass flux were significant; hence, the mean advection and mean vortex force are negligible. The fluctuation advection is the largest in the WEC-only model around the breaking point in both regimes, and its magnitude is weaker in the NW and WEC+CEW models; these model differences are bigger in the marginal regime than in the turbulent regime. Relative to the NW model, the WEC increases the momentum mixing due to eddies around the breaking point, while inclusion of CEW reduces the eddy mixing. The contribution of the fluctuating vortex force $\langle u^{St\prime} \chi' \rangle$ appears only with WEC+CEW; it is generally much smaller than the mean vortex force although it is relatively largest near the shoreline in the turbulent regime.

5.3. Fluctuation Structure

[35] A comparison of time series from the three different models shows the familiar transition between nearly periodic fluctuations and more complex ones (Figure 10; see also Figure 5) in both the waves with CEW and currents in general.

[36] In the marginal regime there is a delay in the onset of the shear instability with CEW compared to the models without CEW because of the suppression for eddy momentum flux (Figures 7c and 8e). The delay due to CEW is also evident in the turbulent regimes although instability develops much more quickly. This delay is qualitatively consistent with OL03 whose fluctuations took longer to develop since they started from resting conditions. There is also a longer oscillation period with CEW. In the marginal regime with fixed μ, the WEC+CEW model time series is nearly periodic, while the NW and WEC-only models show

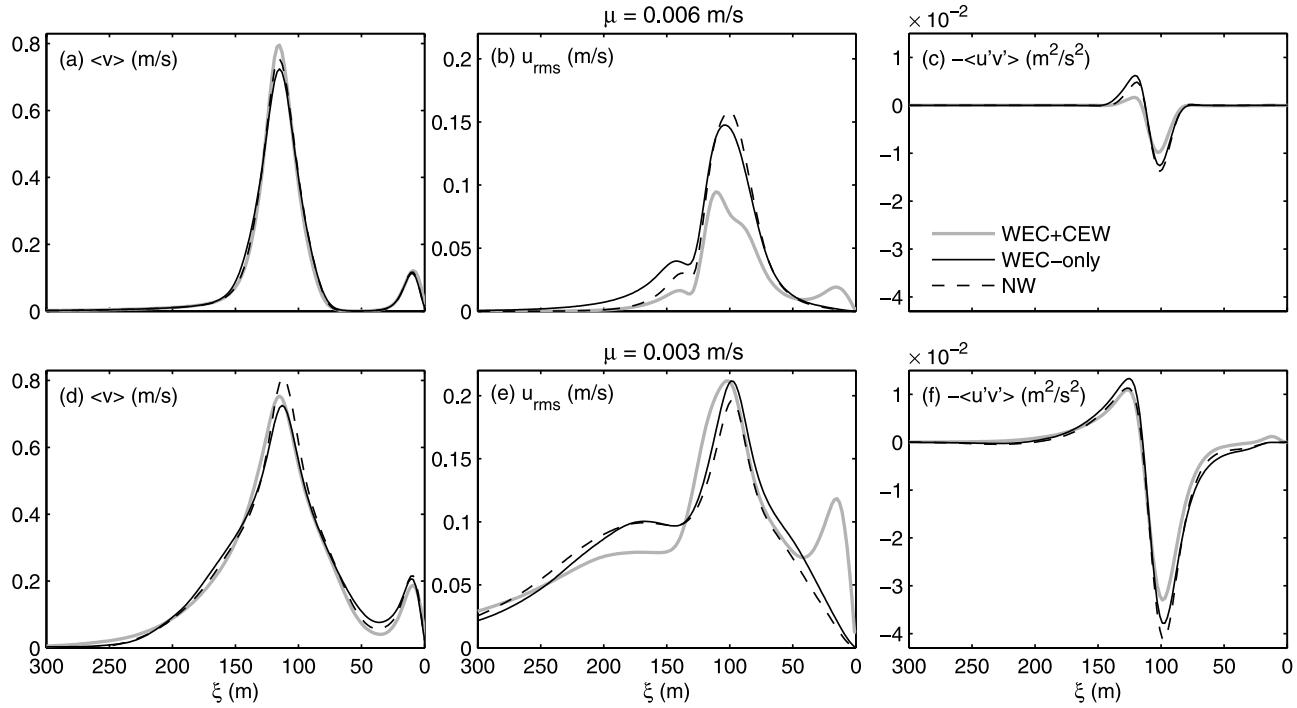

Figure 7. Time- and alongshore-averaged quantities in (a–c) the marginal regime (μ = 0.006 m s^{-1}) and (d–f) the turbulent regime (μ = 0.003 m s^{-1}) for 2-D WEC+CEW, WEC-only, and NW models: Figures 7a and 7d show $\langle v \rangle$, Figures 7b and 7e show fluctuating cross-shore velocity u'_{rms}, and Figures 7c and 7f show Reynolds stress. The time average is for the last 2 h of the 6-h integrations.

evident aperiodicity, consistent with their relative ordering in the fluctuation intensity measures (Figure 7). In the turbulent regime there are similar model differences mainly evident as a broader range of frequencies in the NW and WEC-only models. Notice that $v'(t)$ and $H'_{rms}(t)$ covary almost in phase in the WEC+CEW models.

[37] Vorticity snapshots at t = 6 h give similar indications of the model differences, now expressed in the spatial structure of the fluctuations (Figure 11). In the marginal regime an alongshore meandering pattern is prominent in χ around the breaking points at ξ = 120 m. The wavelength of the meanders is longer in the WEC+CEW model than the other two models, corresponding to the longer period in $v'(t)$. In the turbulent regime longer alongshore spatial scales emerge as current streaks alternating with coherent vortices that roll up from the unstable meanders near the maximum in $\langle v \rangle$. The vortices are ejected as dipoles that carry the two-signed structure of $\langle \chi \rangle$ with them. Offshore cyclonic vortices are closest to circular shapes in the NW model without any wave effects, and they reach farthest offshore in the WEC-only model as agents of its most effective cross-shore eddy momentum flux. Near the shoreline (ξ < 30 m), only the WEC+CEW model has strong eddies (consistent with the statistical profiles in Figure 7). Even in the marginal regime the shoreline eddies are remarkably asymmetric between interiorward cyclonic centers and shoreward anticyclonic meanders, reflecting the proximate flow barrier at the shoreline. In the turbulent regime the strongest nearshore eddies are again cyclones, and they occur quite intermittently in the alongshore direction.

5.4. Alongshore Propagation

[38] Frequency–alongshore wave number spectra are useful to detect celerities associated with the propagating shear waves (Figure 12). A 2-D FFT is applied to $v'(y, t)$ at the bar crest position for the three model formulations, following the technique introduced by *Özkan-Haller and Kirby* [1999]. The spectra are shown with three dispersion curves in each plot: the dispersion relation for lowest-mode edge waves [*Ursell*, 1952] (to exclude them as the explanation for the fluctuations); the mean alongshore current $\langle v \rangle$ (as a Doppler shift influence on the fluctuations); and the fitted shear wave celerity $c^v = f^v/k_y^v$ estimated from the spectrum. In the marginal regime the largest variations occur in a discrete peak around (f^v = 0.0025–0.003 Hz, k_y^v = 0.06–0.007 m^{-1}) and higher harmonics; this reflects the nearly periodic behavior seen in Figures 10 and 11. In the turbulent regime the spectra are broad-banded (Figure 12) but still exhibit a ridge that indicates a dominant celerity value. c^v is similar for all three model formulations, although inclusion of CEW increases c^v relative to the WEC-only model in both regimes. In turn, the vortex force in WEC decreases c^v relative to the NW model (as also demonstrated by *Lane and Restrepo* [2007] in the context of shoreface-connected bar instabilities). The influences of WEC and CEW on propagation are closely related to the magnitude of $\langle v \rangle$. The celerity in the marginal regime closely matches $\langle v \rangle$ at this particular location near the peak in $\langle v \rangle$ (x), but locally fitted c^v values are nearly the same in the x direction for each case (not shown). This implies that the fluctuations move as a coherent mode controlled by a cross-shore-averaged $\langle v \rangle$ over the effective on-offshore span of the fluctuations. The

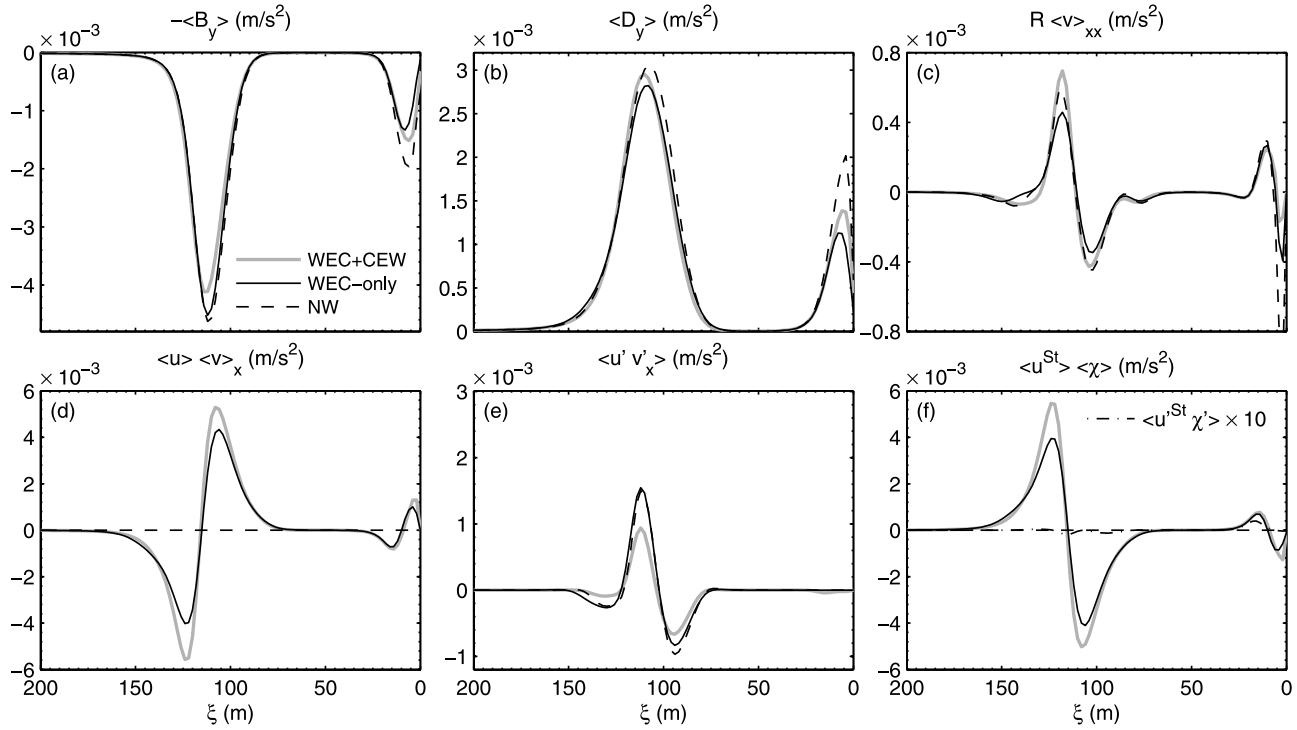

Figure 8. Time- and alongshore-averaged y momentum balance (20) or (23) in the marginal regime (μ = 0.006 m s^{-1}) for 2-D WEC+CEW, WEC-only, and NW models: (a) $\langle B_y \rangle$, (b) bottom drag $\langle D_y \rangle$, (c) lateral viscosity, (d) mean advection, (e) fluctuation advection, and (f) mean vortex force (and fluctuation vortex force only for the WEC+CEW model with a dash-dotted line).

same cross-shore uniformity of c^v is seen in the turbulent regime but to a lesser degree. On the contrary, *Kirby et al.* [2003] and *Noyes et al.* [2005] showed that c^v in the turbulent regime occurs mainly at the local magnitude of $\langle v \rangle$. In principle, noncoherent behavior of the fully nonlinear shear waves may be relevant to the cross-shore variability in c^v, whereas for the linear shear waves inflection point instability excites a single dominant propagation. The weak $\langle v \rangle$ dependency of c^v found here is still an open question, though this contrast may be attributed to the strength of the bottom drag (our turbulent regime result appears to have moderate coherent structure; see Figure 11), incident wave condition, or other unknown factors.

5.5. WEC and CEW in Fluctuation Dynamics

[39] The inclusion of WEC results in an alteration in the magnitude in $-\langle u'v' \rangle$ on both sides of the peak $\langle v \rangle$ (ξ) in both regimes (Figure 7). Further inclusion of CEW reduces u'_{rms} and $-\langle u'v' \rangle$ around the breaking point and increases the fluctuations near the shoreline. To further expose how these effects arise, we Reynolds decompose the advection and vortex force terms in (3) as follows:

$$\mathbf{u} \cdot \nabla \mathbf{u} = \langle \mathbf{u} \rangle \cdot \nabla \langle \mathbf{u} \rangle + \langle \mathbf{u} \rangle \cdot \nabla \mathbf{u}' + \mathbf{u}' \cdot \nabla \langle \mathbf{u} \rangle + \mathbf{u}' \cdot \nabla \mathbf{u}' \quad (25)$$

$$-\hat{\mathbf{z}} \times \mathbf{u}^{St} \chi = -\hat{\mathbf{z}} \times \langle \mathbf{u}^{St} \rangle \langle \chi \rangle - \hat{\mathbf{z}} \times \langle \mathbf{u}^{St} \rangle \chi' - \hat{\mathbf{z}} \times \mathbf{u}^{St\prime} \langle \chi \rangle - \hat{\mathbf{z}} \times \mathbf{u}^{St\prime} \chi'. \quad (26)$$

Terms that are linear in the fluctuations vanish when averaged; alongshore derivatives of mean quantities vanish; both the vortex force terms and $\langle u \rangle$ (= 0) terms are absent in the NW model; and $\mathbf{u}^{St\prime}$ terms are present only in the WEC+CEW model.

[40] The RMS magnitudes of the fluctuating advection terms in the cross-shore component of (25) are displayed in Figure 13 for all three models in the marginal regime. With the WEC and $\langle u \rangle \neq 0$, $\langle u \rangle u'_x$ and $u' \langle u \rangle_x$ contribute substantially, whereas they vanish in the NW model by definition. With CEW the dominant alongshore advection by $\langle v \rangle u'_y$, as well as the eddy Reynolds stress divergence contributions $u'u'_x$ and $v'u'_y$, are greatly reduced since u'_{rms} is weaker compared to WEC-only (Figure 7b). Analogous fluctuating vortex force terms for the WEC models (Figure 14) have somewhat smaller amplitudes than the advection terms except nearshore. The vortex force terms $\propto v^{St\prime}$ that arise only in CEW models are smaller than $\langle v^{St} \rangle \chi'$ in the marginal regime offshore but comparable nearshore. In the turbulent regime $v^{St\prime} \chi'$ is comparable offshore and even dominant nearshore where it is a principal source of u' variability (but also see B_x; see below).

[41] Next we focus on the spatial structure of the cross-shore velocity fluctuation, Reynolds stress, WEC advective tendency ($-\langle u \rangle u'_x$ and $-u' \langle u \rangle_x$), and a component of cross-shore VF, $\langle v^{St} \rangle \chi'$ (Figure 15). Coinciding with the locations of peak cross-shore flow in the shear waves, the Reynolds stress and an advective term $-\langle u \rangle u'_x$ change sign in the cross-shore direction as does the other advective term, $-u' \langle u \rangle_x$, which is somewhat weaker; see also Figure 13. This behavior is consistent with the enhanced positive and negative Reynolds stress values on the offshore and inshore sides of the peak in $\langle v \rangle$ with the WEC seen in Figure 7.

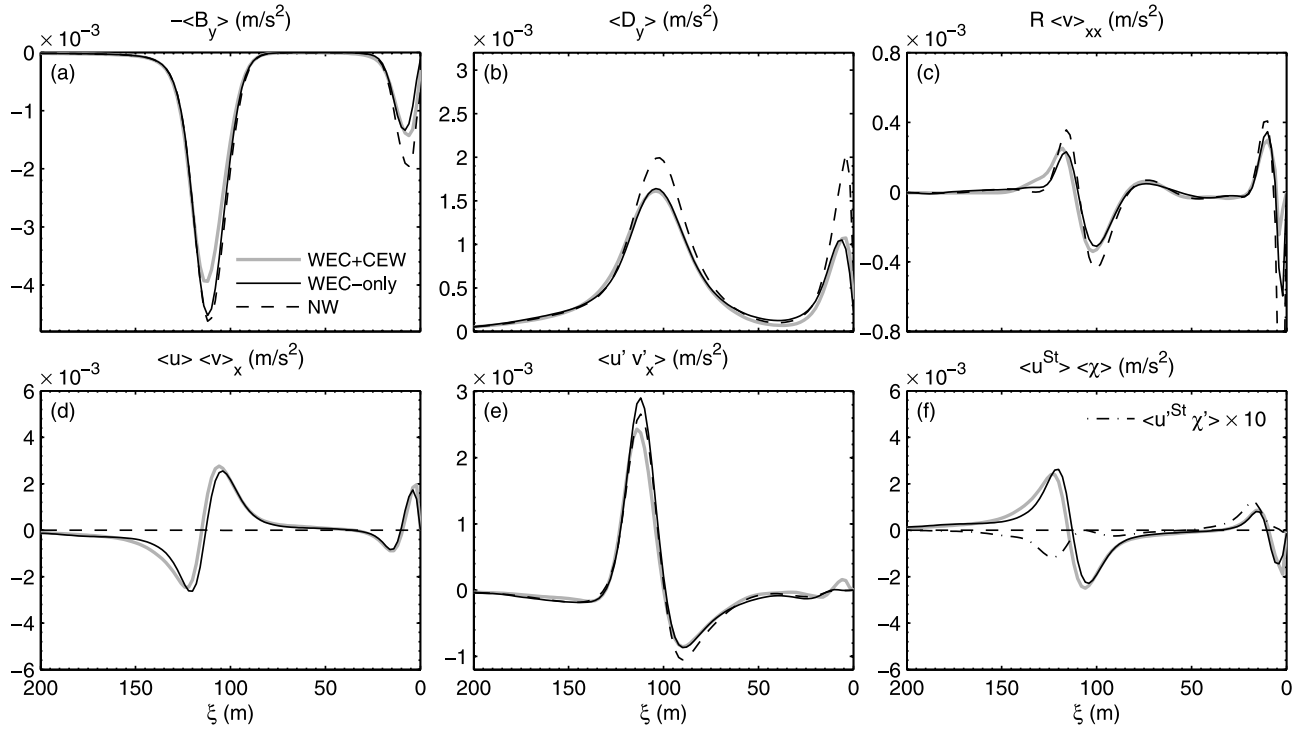

Figure 9. The same as Figure 8 except in the turbulent regime (μ = 0.003 m s^{-1}).

These advective tendency terms act to strongly accentuate u' on the offshore side and more weakly deplete it on the inshore side. Meanwhile, the cross-shore vortex force term $\langle v^{St} \rangle \chi'$ varies approximately in phase with u' and further acts to strengthen the instability. These WEC characterizations are also valid in the turbulent regime (not shown).

[42] To further isolate the influences of CEW, two wave simulations with and without CEW are performed to evaluate terms in the momentum equation (3) while fixing the current field to be that of the WEC-only model. Instantaneous u and simulation differences are plotted in Figure 16. The waves are significantly modified by both anti-Stokes mean flow and shear wave refraction. Ray focusing occurs in offshore-directed flow regions and increases H_{rms} in the adjacent runnel; conversely, ray divergence occurs in shoreward flow regions and decreases the runnel H_{rms}. The net increase of H_{rms} with CEW implies an energy transfer from the offshore-directed flows associated with the shear waves (as remarked by OL03). In addition, wave refraction also occurs on the anti-Stokes current (Figure 4) with the present formalism. These current effects are somewhat analogous to shoaling for the incident waves. The modifications to H_{rms} and θ lead to meandering in the breaking acceleration **B** and in **J**. CEW enhances the shoreward B_x around the breaking

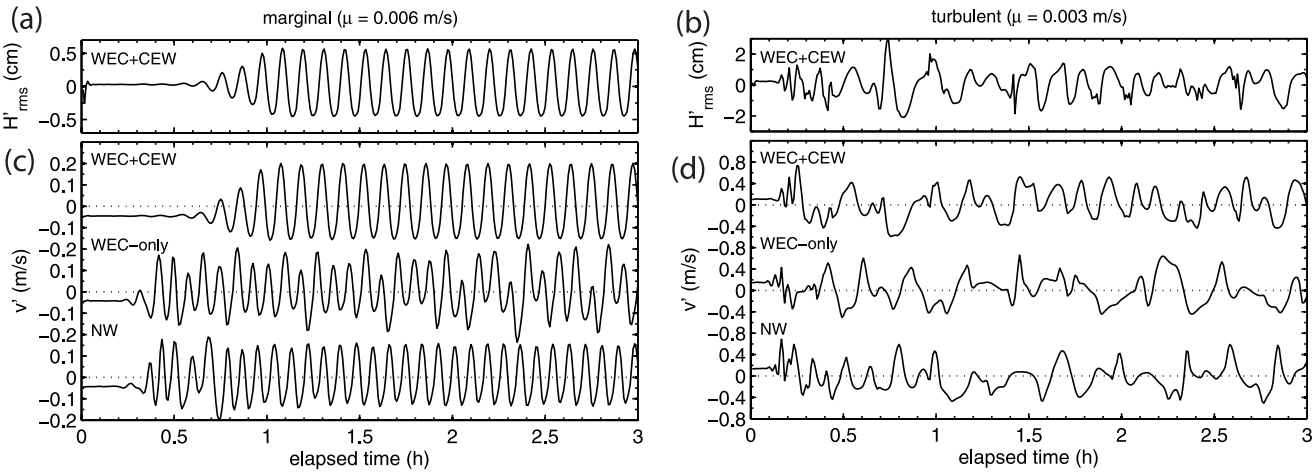

Figure 10. Time series (a and b) of fluctuating H_{rms} in the WEC+CEW model and (c and d) of v' in the three models at the bar crest (ξ, y) = (100 m, 384 m). Marginal regimes (μ = 0.006 m s^{-1}) are shown in Figures 10a and 10c, and turbulent regimes (μ = 0.003 m s^{-1}) are shown in Figures 10b and 10d.

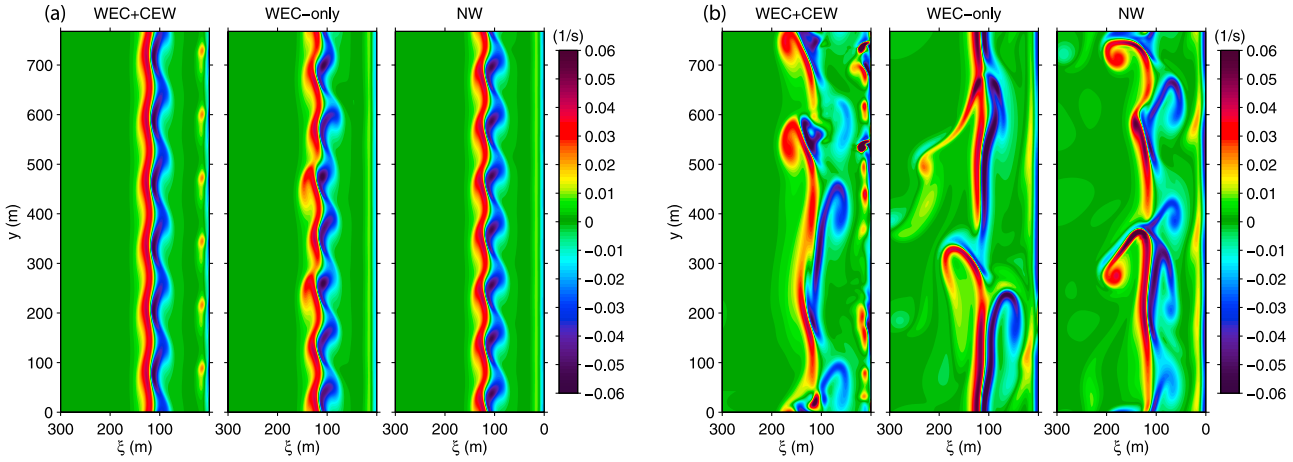

Figure 11. Instantaneous vorticity χ for WEC + CEW, WEC-only, and NW models at t = 6 h. (a) Marginal (μ = 0.006 m s^{-1}) and (b) turbulent (μ = 0.003 m s^{-1}) regimes.

point off the bar crest and in the shoreline region by about 15% of their peak values to oppose the instantaneous u headed offshore. Conversely, the change in ΔB_x is negative in onshore flow regions. This extra breaking acceleration opposes the shear wave cross-shore flow and acts to suppress it, with the evident CEW consequences of delayed instability onset (Figure 10) and reduced velocity fluctuation amplitude and Reynolds stress (Figure 7). The shoreline CEW consequences in B_x are even more striking with intense shoreward accelerations at the ray focal centers.

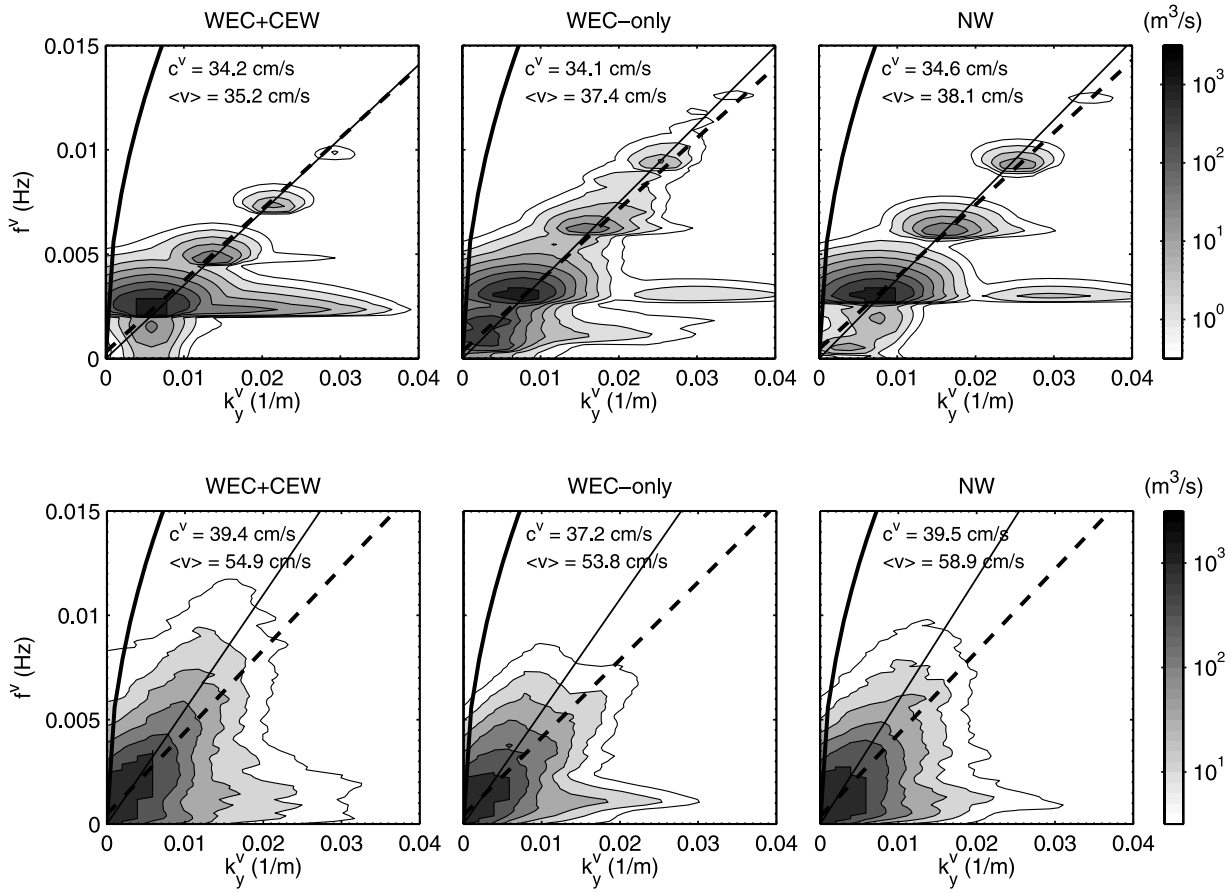

Figure 12. Frequency–alongshore wave number spectra for v' at the bar crest (ξ = 100 m) in the (top) marginal and (bottom) turbulent regimes for WEC+CEW, WEC-only, and NW models. Thick solid lines are the dispersion curves for the lowest edge mode (as estimated by *Ursell* [1952]), thin solid lines are time- and alongshore-averaged $\langle v \rangle$, and dashed lines are the inferred shear wave celerity c^v.

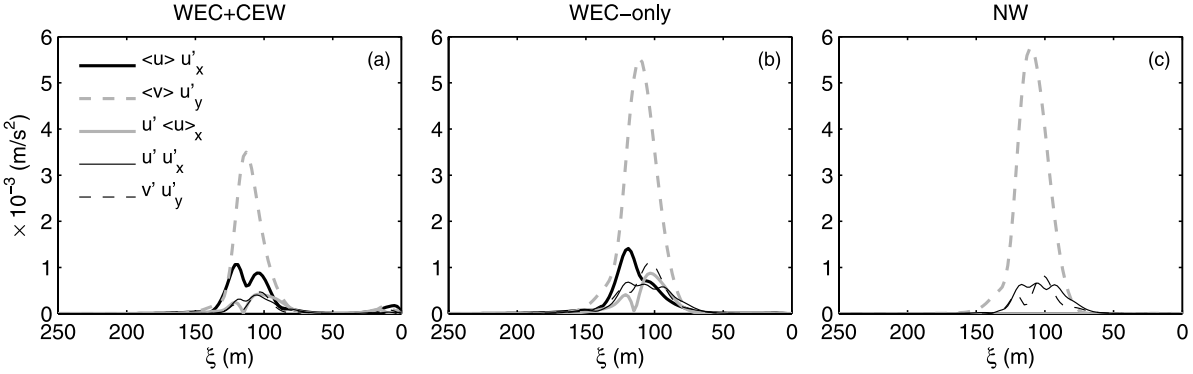

Figure 13. Cross-shore profiles of the RMS Reynolds-decomposed advection terms in the cross-shore momentum balances (3) and (18) for the marginal regime (μ = 0.006 m s^{-1}).

[43] The CEW alterations to the wave field also influence B_y in phase with the shear waves. ΔB_y has positive and negative values in phase with the θ anomalies, both in the offshore region and near the shoreline. $\langle \Delta B_y \rangle$ is negative around the bar crest and positive near the shoreline, consistent with Figures 8 and 9. This effects a net transfer of alongshore momentum from the bar to the shore by diminishing the breaking near the bar that subsequently must increase at the shore since the total wave energy must be dissipated. Thus, both B_x and B_y are increased near the shoreline, leading to the greatly enhanced fluctuations there in the WEC+CEW model. Finally, CEW increases ΔJ_x by about 40% and ΔJ_y by about 6% of their offshore maxima in the WEC-only model; however, these vortex force terms are much smaller than the breaking acceleration terms, hence of lesser influence as agents of CEW on $\mathbf{u}'$.

6. Concluding Remarks

[44] Wave breaking acceleration is well understood to be a cause of littoral currents, with bottom drag providing the primary equilibrating balance, even though the alongshore vortex force and anti-Stokes momentum advection also contribute. In this paper we show that wave-current interactions significantly influence the littoral shear instability phenomenon that mostly has been understood without these interactions. Some of our conclusions are implicit in the radiation stress and current refraction model of OL03, but here we give them an explicit interpretation in our WEC+CEW model formulation partly by separating **B** and **J**.

[45] The WEC enhance offshore shear instability and its attendant eddy momentum flux, thereby weakening and spreading the mean littoral current $\langle v \rangle$ (x) near the offshore bar. It does this partly through the advective influence of a mean cross-shore anti-Stokes flow $\langle u \rangle$. The combined WEC+CEW delay the onset of instability, suppresses cross-shore velocity fluctuations, weakens breaking near the bar, and diminishes eddy momentum flux, leading to a stronger, narrower $\langle v \rangle$. The WEC + CEW also energizes the fluctuations in the nearshore region by refracting the gravity wave rays around the shear wave meanders and modulating the breaking near the shoreline.

[46] The onshore increase in cross-shore breaking acceleration is potentially even more important for offshore-directed flows associated with rip currents over an alongshore-varying topography. This has been reported by *Yu and Slinn* [2003] with a coupled wave-current modeling framework similar to that given by OL03, where the CEW influence on breaking effects significantly reduces the offshore extent of the rip currents. This behavior is also being investigated with our formalism and will be reported separately.

[47] We use the bottom drag parameterization to control successive instability regime transitions to weakly unstable and complex fluctuation behaviors (as also done previously).

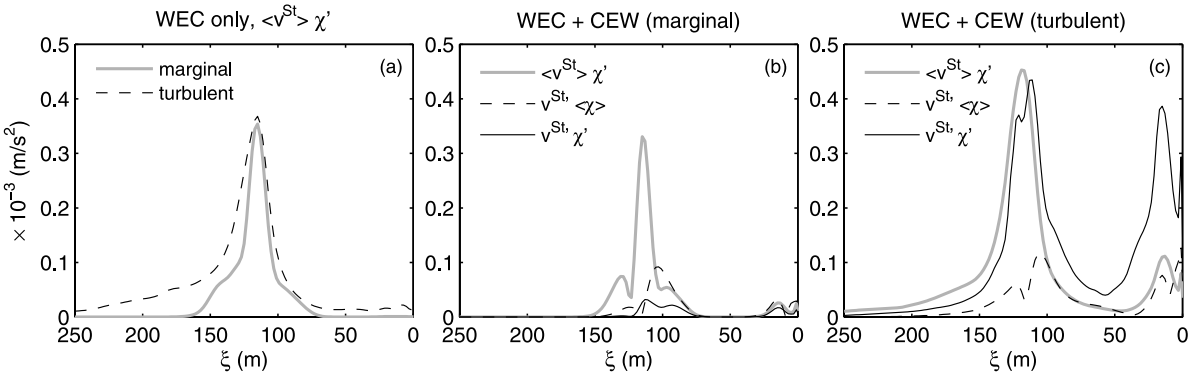

Figure 14. Cross-shore profiles of the RMS Reynolds-decomposed vortex force terms in the cross-shore momentum equation (3): (a) $\langle v^{St} \rangle \chi'$ for the WEC-only model in the marginal and turbulent regimes (μ = 0.006 and 0.003 m s^{-1}) and $\langle v^{St} \rangle \chi'$, $v^{St\prime} \langle \chi \rangle$, and $v^{St\prime} \chi'$ for the WEC+CEW model in (b) the marginal and (c) turbulent regimes.

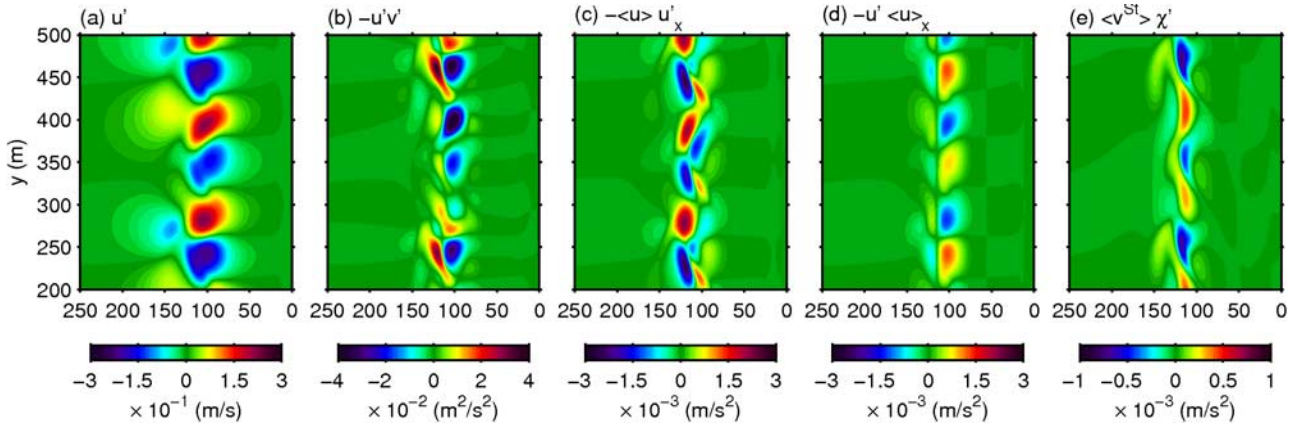

Figure 15. WEC-only model snapshots of instantaneous quantities at t = 6 h in the marginal regime (μ = 0.006 m s^{-1}): (a) fluctuating cross-shore velocity u'; (b) Reynolds stress $-u'v'$; (c) cross-shore advection of u', $-\langle u\rangle u'_x$; (d) cross-shore advection of $\langle u\rangle$, $-u'\langle u\rangle_x$; and (e) cross-shore VF contribution from χ', $\langle v^{St}\rangle\ \chi'$. Notice that the scales are not the same.

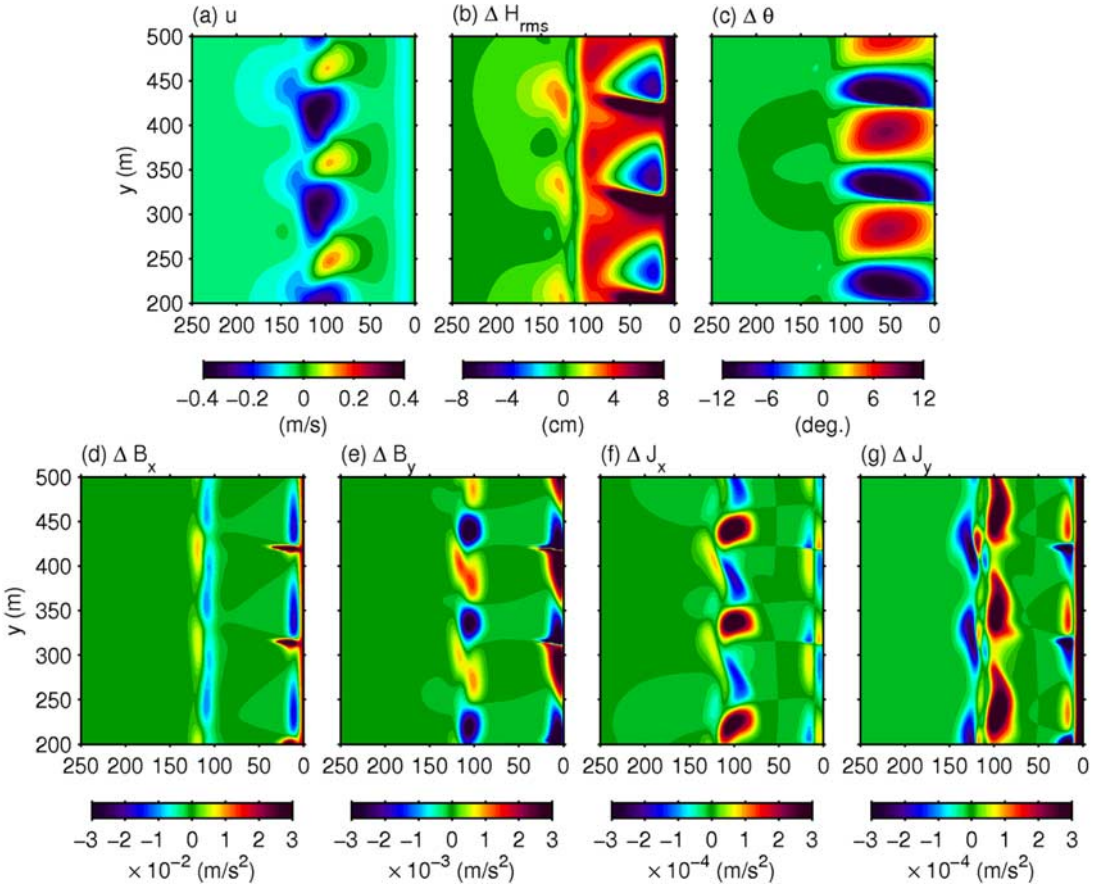

Figure 16. Instantaneous quantities in the marginal regime (μ = 0.006 m s^{-1}) at t = 12 h. (a) The WEC-only cross-shore velocity u and differences diagnostically calculated with and without CEW using the same **u** field: (b) ΔH_{rms}, (c) $\Delta\theta$, (d) ΔB_x, (e) ΔB_y, (f) ΔJ_x, and (g) ΔJ_y.

This control is cleanest with a decreasing coefficient μ with a linear current drag law. On the basis of the spectral plots, qualitatively similar behaviors occur with the nonlinear, wave-current drag laws by *Soulsby* [1995] and *Feddersen et al.* [2000], that mimic high- and low-μ regimes, respectively.

[48] **Acknowledgments.** We appreciate the support from the National Science Foundation (DMS-0723757) and Office of Naval Research (N00014-04-1-0166). We also appreciate the help of Emily Lane and Brad Weir in code preparation and preliminary calculations. Thanks are also due to two anonymous reviewers and James Kirby for their constructive comments and suggestions.

References

Allen, J. S., P. A. Newberger, and R. A. Holman (1996), Nonlinear shear instabilities of alongshore currents on plane beaches, *J. Fluid Mech.*, *310*, 181–213.

Bowen, A. J., and R. A. Holman (1989), Shear instabilities of the mean longshore current: 1. Theory, *J. Geophys. Res.*, *94*, 18,023–18,030.

Bowen, A. J., D. L. Inman, and V. P. Simmons (1968), Wave "set-down" and wave setup, *J. Geophys. Res.*, *73*, 2569–2577.

Bühler, O., and T. E. Jacobson (2001), Wave-driven currents and vortex dynamics on barred beaches, *J. Fluid Mech.*, *449*, 313–339.

Chen, Q., J. T. Kirby, R. A. Dalrymple, F. Shi, and E. B. Thornton (2003), Boussinesq modeling of longshore currents, *J. Geophys. Res.*, *108*(C11), 3362, doi:10.1029/2002JC001308.

Church, J. C., and E. B. Thornton (1993), Effects of breaking wave induced turbulence within a longshore current model, *Coastal Eng.*, *20*, 1–28.

Craik, A. D. D., and S. Leibovich (1976), A rational model for Langmuir circulations, *J. Fluid Mech.*, *73*, 401–426.

Dodd, N., J. Oltman-Shay, and E. B. Thornton (1992), Shear instabilities in the longshore current: A comparison of observation and theory, *J. Phys. Oceanogr.*, *22*, 62–82.

Dodd, N., J. Oltman-Shay, and E. B. Thornton (1994), On the destabilization of a longshore current on a plane beach: Bottom shear stress, critical condition and onset of instabilities, *J. Geophys. Res.*, *99*, 811–824.

Dodd, N., V. Iranzo, and A. Reniers (2000), Shear instabilities of wave-driven alongshore currents, *Rev. Geophys.*, *38*, 437–464.

Feddersen, F. (1998), Weakly nonlinear shear waves, *J. Fluid Mech.*, *372*, 71–91.

Feddersen, F., R. Guza, S. Elgar, and T. Herbers (2000), Velocity moments in alongshore bottom stress parameterizations, *J. Geophys. Res.*, *105*, 8673–8686.

Flather, R. A. (1976), A tidal model of the northwest european continental shelf, *Mem. Soc. R. Sci. Liege*, *6*, 141–164.

Hasselmann, K. (1971), On the mass and momentum transfer between short gravity waves and larger-scale motions, *J. Fluid Mech.*, *50*, 189–201.

Kennedy, A. B., and Y. Zhang (2008), The stability of wave-driven rip current circulation, *J. Geophys. Res.*, *113*, C03031, doi:10.1029/2006JC003814.

Kirby, J. T., Q. Chen, T. J. Noyes, R. T. Guza, and S. Elgar (2003), Evaluating the low frequency predictions of a Boussinesq wave model: Field cases, in *The Proceedings of the Thirteenth (2003) International Offshore and Polar Engineering Conference*, vol. III, edited by J. S. Chung et al., pp. 396–402, Int. Soc of Offshore and Polar Eng., Cupertino, Calif.

Lane, E. M., and J. M. Restrepo (2007), Shoreface-connected ridges under the action of waves and currents, *J. Fluid Mech.*, *582*, 23–52.

Lane, E. M., J. M. Restrepo, and J. C. McWilliams (2007), Wave-current interaction: A comparison of radiation-stress and vortex-force representations, *J. Phys. Oceanogr.*, *37*, 1122–1141.

Longuet-Higgins, M. S. (1970a), Longshore currents generated by obliquely incident sea waves, 1, *J. Geophys. Res.*, *75*(33), 6778–6789.

Longuet-Higgins, M. S. (1970b), Longshore currents generated by obliquely incident sea waves, 2, *J. Geophys. Res.*, *75*(33), 6790–6801.

Longuet-Higgins, M. S., and R. W. Stewart (1962), Radiation stress and mass transport in gravity waves, with application to "surf beats", *J. Fluid Mech.*, *13*, 481–504.

Longuet-Higgins, M. S., and R. W. Stewart (1964), Radiation stresses in water waves: A physical discussion, with applications, *Deep Sea Res.*, *11*, 529–562.

McWilliams, J. C., and J. M. Restrepo (1999), The wave-driven ocean circulation, *J. Phys. Oceanogr.*, *29*, 2523–2540.

McWilliams, J. C., P. P. Sullivan, and C.-H. Moeng (1997), Langmuir turbulence in the ocean, *J. Fluid Mech.*, *334*, 1–30.

McWilliams, J. C., J. M. Restrepo, and E. M. Lane (2004), An asymptotic theory for the interaction of waves and currents in coastal waters, *J. Fluid Mech.*, *511*, 135–178.

Newberger, P., and J. S. Allen (2007), Forcing a three-dimensional, hydrostatic, primitive-equation model for application in the surf zone: 2. Application to DUCK94, *J. Geophys. Res.*, *112*, C08019, doi:10.1029/2006JC003474.

Noyes, T. J., R. T. Guza, F. Feddersen, S. Elgar, and T. H. C. Herbers (2005), Model-data comparisons of shear waves in the nearshore, *J. Geophys. Res.*, *110*, C05019, doi:10.1029/2004JC002541.

Oltman-Shay, J., P. A. Howd, and W. A. Birkemeier (1989), Shear instabilities of the mean longshore current: 2. Field observations, *J. Geophys. Res.*, *94*, 18,031–18,042.

Özkan-Haller, H. T., and J. T. Kirby (1999), Nonlinear evolution of shear instabilities of the longshore current: A comparison of observations and computations, *J. Geophys. Res.*, *104*, 25,953–25,984.

Özkan-Haller, H. T., and Y. Li (2003), Effects of wave-current interaction on shear instabilities of longshore currents, *J. Geophys. Res.*, *108*(C5), 3139, doi:10.1029/2001JC001287.

Raubenheimer, B., R. T. Guza, and S. Elgar (2001), Field observation of wave-driven setdown and setup, *J. Geophyis. Res.*, *106*(C3), 4629–4638.

Reniers, A. J. H. M., J. A. Battjes, A. Falqués, and D. A. Huntley (1997), A laboratory study on the shear instability of logngshore currents, *J. Geophys. Res.*, *102*, 8597–8609.

Ruessink, B., J. Miles, F. Feddersen, R. Guza, and S. Elgar (2001), Modeling the alongshore current on barred beach, *J. Geophys. Res.*, *106*(C10), 22,451–22,463.

Shchepetkin, A. F., and J. C. McWilliams (2005), The Regional Oceanic Modeling System: A split-explicit, free-surface, topography-following-coordinate oceanic model, *Ocean Modell.*, *9*, 347–404.

Slinn, D. N., J. S. Allen, P. A. Newberger, and R. A. Holman (1998), Nonlinear shear instabilities of alongshore currents over barred beaches, *J. Geophys. Res.*, *103*, 18,357–18,379.

Smith, J. (2006), Wave-current interactions in finite depth, *J. Phys. Oceanogr.*, *36*, 1403–1419.

Soulsby, R. L. (1995), Bed shear-stresses due to combined waves and currents, in *Advances in Coastal Morphodynamics*, edited by M. Stive et al., pp. 4-20–4-23, Delft Hydraul., Delft, Netherlands.

Soulsby, R. L. (1997), *Dynamics of Marine Sands, A Manual for Practical Applications*, 249 pp., Thomas Telford, London.

Terrile, E., M. Brocchini, K. H. Christensen, and J. T. Kirby (2008), Dispersive effects on wave-current interaction and vorticity transport in nearshore flow, *Phys. Fluid*, *20*, 036602, doi:10.1063/1.2888973.

Thornton, E. B, and R. T. Guza (1983), Transformation of wave height distribution, *J. Geophys. Res.*, *88*(C10), 5925–5938.

Thornton, E. B., and R. T. Guza (1986), Surf zone longshore currents and random waves: Field data and models, *J. Phys. Oceanogr.*, *16*, 1165–1178.

Uchiyama, Y., and J. C. McWilliams (2008), Infragravity waves in the deep ocean: Generation, propagation, and seismic hum excitation, *J. Geophys. Res.*, *113*, C07029, doi:10.1029/2007JC004562.

Ursell, F. (1952), Edge waves on a sloping beach, *Proc. R. Soc. London, Ser. A*, *214*, 79–97.

Yu, J., and D. N. Slinn (2003), Effects of wave-current interaction on rip currents, *J. Geophys. Res.*, *108*(C3), 3088, doi:10.1029/2001JC001105.

J. C. McWilliams and Y. Uchiyama, Institute of Geophysics and Planetary Physics, University of California, Los Angeles, CA 90095-1565, USA. (uchiyama@atmos.ucla.edu)

J. M. Restrepo, Department of Mathematics, University of Arizona, Tucson, AZ 85721, USA.